



Understanding electrochemical potentials of cathode materials in rechargeable batteries

Chaofeng Liu¹, Zachary G. Neale² and Guozhong Cao^{1,2,*}

¹Beijing Institute of Nanoenergy and Nanosystems, Chinese Academy of Sciences, Beijing 100083, China

²Department of Materials Science and Engineering, University of Washington, Seattle 98195, WA, USA

Presently, sustainable energy as well as efficient and economical energy conversion and storage technologies has become important work in light of the rising environmental issues and dependence on portable and uninterrupted power sources. Increasingly more researchers are focusing on harvesting and converting solar energy, mechanical vibration, waste heat, and wind to electricity. Electrical energy storage technologies play a significant role in the demand for green and sustainable energy.

Rechargeable batteries or secondary batteries, such as Li-ion batteries, Na-ion batteries, and Mg-ion batteries, reversibly convert between electrical and chemical energy via redox reactions, thus storing the energy as chemical potential in their electrodes. The energy density of a rechargeable battery is determined collectively by the specific capacity of electrodes and the working voltage of the cell, which is the differential potential between the cathode and the anode. Over the past decades, a significant number of studies have focused on enhancing this specific capacity; however, studies to understand and manipulate the electrochemical potential of the electrode materials are limited. In this review, the material characteristics that determine and influence the electrochemical potentials of electrodes are discussed. In particular, the cathode materials that convert electricity and chemical potential through electrochemical intercalation reactions are investigated. In addition, we summarize the selection criteria for elements or compounds and the effect of the local atomic environment on the discharge potential, including the effects of site energy, defects, crystallinity, and microstructure, using LiMn_2O_4 , V_2O_5 , Mo_6S_8 , LiFePO_4 , and LiCoO_2 as model samples for discussion.

Introduction

In addition to the rising concern of environmental pollution, modern society is becoming increasingly dependent on uninterrupted portable power sources for continuous Internet access and for working or collaborating with people across the globe. In spite of the efforts of both the research community and industries, the development of portable power devices has been painstakingly slow [1,2], falling behind the rapid advancements in electronic devices and electrically powered instruments and infrastructure. The industrial revolutions in the past centuries have led to unprecedented changes in social life, transportation, and production

activities, with energy utilization reflecting the progress of industrial technology and human civilization. Fossil fuels, such as coal, crude oil, and natural gas, are used as primary energy sources to power all high-tech-dependent human activities. However, pollution arising from fossil fuel combustion has had a devastating impact on human health and the natural environment [3,4]. In addition, regardless of governmental policies or the fluctuation in price and supply, the natural reserves of fossil fuels are limited and not sustainable. Therefore, the focus of research has shifted to environmentally benign sustainable energy. Clean energy can be divided into three components: harvest and conversion of sustainable clean energy including solar energy, wind, mechanical vibration, and waste heat; energy storage typically in the form of

*Corresponding author: Cao, G. (gzcao@u.washington.edu)



FIGURE 1

The energy utilization chain. Efficient harvest, storage, and management are three essential segments to energy consumption in modern society [5,33].

chemical potential including batteries, hydrogen, and biofuels; and management and efficient usage of energy including smart buildings and efficient lighting systems [5–10] (Fig. 1). Typical energy storage technologies, particularly for portable electronics and mobile instruments, are based on the conversion of electricity and chemical potential, as seen in fuel cells, batteries, and electrochemical pseudocapacitors, with the energy being stored in the form of chemical potential [6,11–13].

Due to their high energy density, batteries have long been used [14] to power portable electronics, as well as stationary and mobile instruments [15], such as lead acid batteries for automobiles [16]. In the last two decades, Li-ion batteries have advanced rapidly with increased energy density and long cyclic stability, which is beneficial for most portable electronics including mobile phones and laptop computers [16–19]. Current rechargeable batteries based on ion insertion/extraction in electrodes, including Li- [20–22], Na- [23–25], Mg- [18,26,27], and Al-ion [28,29] batteries, have been increasingly studied in both the academia and industry. However, sodium, magnesium, and aluminum have a lesser reducing effect than lithium (–2.71, –2.37, and –1.66 V vs. S.H.E., respectively, compared with –3.04 V for Li) as well as low gravimetric capacities (1165, 2046, and 2978 mAh/g, respectively; compared with lithium, 3850 mAh g⁻¹). Thus, devices based on metallic sodium, magnesium, or aluminum anodes have lower energy densities and operating voltages than those with lithium metal anodes [25,26,28]. To date, only Li-ion rechargeable batteries have been successfully commercialized and become an irreplaceable power source. In Li-ion rechargeable batteries, the cathodes that store lithium ions via electrochemical intercalation must contain suitable lattice sites or spaces to store and release working ions reversibly. Robust crystal structures with sufficient storing sites are required to produce a material with stable cyclability and high specific capacity [24,30]. In addition, a cathode with high electrochemical intercalation potential can be used to develop a high energy density battery with a given anode. This is because the energy density of the device equals the product of the specific capacity of the electrode materials and the working voltage that is determined by the differential electrochemical potentials between

the cathode and anode [22,31]. This review focuses on secondary Li-ion batteries and their components to illustrate certain fundamental factors, in particular, the origin of the electrochemical potential of electrode materials and effective approaches to exploiting these electrochemical properties. In addition, the potential electrode materials for Na- and Mg-ion batteries are also discussed as the fundamental understanding acquired on Li-ion batteries will greatly benefit the increasing efforts on Na- and Mg-ion battery research [32].

Configuration and principle of Li-ion batteries

Li-ion rechargeable batteries consist of two electrodes, anode and cathode, immersed in an electrolyte and separated by a polymer membrane (Fig. 2). This basic device configuration has remained unchanged from the earliest developed batteries [34]. The similarities between Li-ion batteries and conventional batteries include the redox reactions at the interfaces between the electrolyte and electrodes, accompanied by the diffusion of ions in the electrolyte. However, the differences between conventional batteries, or galvanic cells, and Li-ion batteries are notable as well. In typical galvanic batteries, the redox reactions proceed simultaneously with the receding or advancing of the electrode surfaces, but not accompanied by either the solid-state mass diffusion in the electrodes or a change in the chemical composition and local atomic environment [35]. By contrast, the heterogeneous redox reactions in Li-ion batteries are always accompanied by solid-state

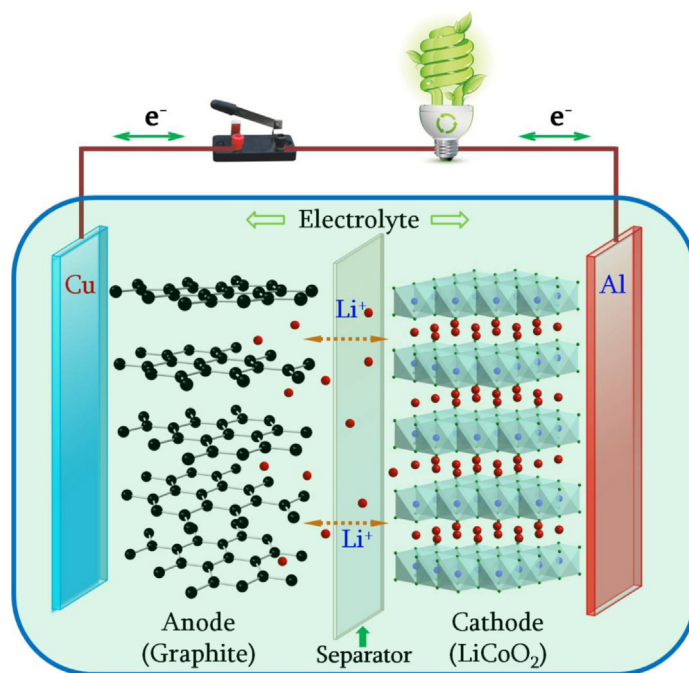


FIGURE 2

Schematic of the configuration of rechargeable Li-ion batteries. Na-ion, Mg-ion, or Al-ion batteries also have similar configurations, which differ from electrode materials [29,70,71]. For a Li-ion battery, as illustrated in the figure, Li ions are extracted from the cathode and inserted into the anode during the charge process, and the reverse reaction occurs during the discharge process. However, in a half-cell consisting of electrode material and lithium metal, Li ions are extracted from the electrode material and deposited on the surface of the lithium metal during the charge process, and Li ions are inserted into the host electrode material during discharge. Here, in practice, the electrode materials can be cathodes or anodes.

mass diffusion as well as volume expansion or contraction, although the electrode surfaces do not recede or advance when the volume change of electrodes is not considered. Therefore, it is very reasonable that researchers face different challenges when developing Li-ion batteries, necessitating different fundamental considerations. Li ions, the working ionic component of electrochemical reactions, are transferred back and forth between the anode and the cathode through the electrolyte. While the concentration of lithium ions remains constant in the electrolyte regardless of the degree of charge or discharge, it varies in the cathode and anode with the charge and discharge states. The storage of lithium ions in electrodes occurs via three types of electrochemical reactions: (1) alloying such as silicon and tin [36–38]; (2) conversion such as CuO and SnO₂ [39]; and (3) intercalation such as graphite, LiCoO₂, and V₂O₅ [39–41]. Alloying offers a specific capacity several times to more than an order of magnitude greater than that of other reaction mechanisms, although it results in a large volume change, typically more than 100% [5,36]. Conversion reactions are often limited by their irreversibility, thus requiring small particle sizes, typically less than 20 nm in diameter [42]. Therefore, conversion reactions are often combined with alloying [21], but they are rarely used alone in lithium-ion batteries. Electrochemical intercalation reactions are widely applied in Li-ion batteries for both anodes, such as graphite [43,44], and cathodes, such as LiCoO₂ [45] and LiFePO₄ [46,47]. Intercalation reactions require the host electrode material to possess space to accommodate Li ions as well as multivalent ions to maintain the electroneutrality. The compounds most commonly studied and widely used for Li-ion intercalation are transition metal-containing compounds with layered, spinel, or olivine structures [30,48]. The cathode, anode, and electrolyte are the most important active materials that determine the performance of a Li-ion battery. As anode materials offer a higher Li-ion storage capacity than cathodes do, the cathode material is the limiting factor in the performance of Li-ion batteries [1,41]. The energy density of a Li-ion battery is often determined collectively by the Li-ion storage capacity and the discharge potential of the cell. The factors determining the Li-ion storage capacity through intercalation are as follows: (1) the capability of the host, or the electrode, to change the valence states; (2) the available space to accommodate the Li ions; and (3) the reversibility of the intercalation reactions. The discharge potential of a cathode is directly proportional to the reduction of Gibbs free energy when Li ions are inserted into the electrode [49,50], which is discussed in detail in the following section.

The energy density and power density of a battery are two parameters essential to evaluating its practical performance, and they are commonly presented in Ragone plots [51]. Although batteries offer a much higher energy density than electric double-layer capacitors (EDLCs), also often referred to as supercapacitors or ultracapacitors, and electrochemical pseudocapacitors, they possess relatively lower power density and shorter cyclic life [11,52]. A significant number of studies have been conducted on the synthesis and characterization of various nanostructured cathode and anode materials with large specific surface area and short solid-state transport distance, offering an enhanced power density as well as a better cyclic stability [53,54]. The energy storage performance has been enhanced by conformally applying a thin (typically a couple of nanometers) and porous carbon film (with a

pore size of a few nanometers or less) on nanostructured cathode or anode materials [55–57]. Other carbon materials including carbon nanotubes, graphene, and graphene oxide have been introduced into electrodes as electrically conductive additives, structural stabilizers, reactive precursors, or catalysts/promoters, leading to a significant enhancement in the electrical energy storage performance of electrodes and batteries [58–61]. A high power density can also be obtained by fabricating hybrid supercapacitor batteries [51,62]. However, enhancement of the energy density in a battery is limited by the lithium-ion storage capacity and the cell potential. The storage capacity is determined by the amount of lithium ions that can be reversibly inserted and extracted through a reversible first-order phase transition in intercalation reactions under the operating conditions of the battery [63,64]. The electrochemical potential varies with the materials in question, showing a direct correlation with their electronic configuration. Considerable research efforts have been devoted to achieving large specific capacity, good cyclic stability, and high rate capability in electrode materials [65–69]. However, experimental studies on controlling and tuning the electrochemical potentials of electrode materials are limited, although some notable theoretical studies have calculated and analyzed electrochemical potentials based on the electronic structure and atomistic potentials [50]. The cell voltage and electrochemical potentials of electrode materials can provide insight for designing and developing suitable materials for batteries with high energy density in the future.

Voltage of a battery

Cell voltage is determined by the compatibility of the whole system, including the anode, cathode, and electrolyte. In particular, the difference in chemical potential between the anode (μ_A) and the cathode (μ_C) is termed as the working voltage, also known as the open circuit voltage, V_{OC} [31,47]:

$$V_{OC} = \frac{(\mu)_A - \mu_C}{e} \quad (1)$$

where e is the magnitude of the electronic charge. This working voltage is also limited by the electrochemical window of the electrolyte, which, as illustrated in Fig. 3a, is determined by the energy gap from the highest occupied molecular orbital (HOMO) to the lowest unoccupied molecular orbital (LUMO). The anode and cathode must be selected such that the μ_A of the anode lies below the LUMO and the μ_C of the cathode is located above the HOMO; otherwise, the electrolyte will be reduced on the anode or oxidized on the cathode to form a passivating solid electrolyte interphase (SEI) film [2,72]. It is worth noting that this SEI film permits the diffusion of Li ions through the film under a uniform electric field and reduces the overpotential and concentration polarization [49]. The SEI can also prevent the aggregation of electrochemically active particles and maintain a uniform chemical composition at the electrodes. For example, the SEI can effectively prevent the exfoliation of graphite during the insertion and extraction of lithium ions [73]. However, the SEI film increases the internal resistance of the battery and consumes part of the Li ions from the cathode, leading to both power and capacity loss [49]. In addition to the electrochemical window of the electrolyte, the p electron band of anions also determines the achievable voltage in the cathode. The anion (O^{2-}) will undergo oxidation to form gas

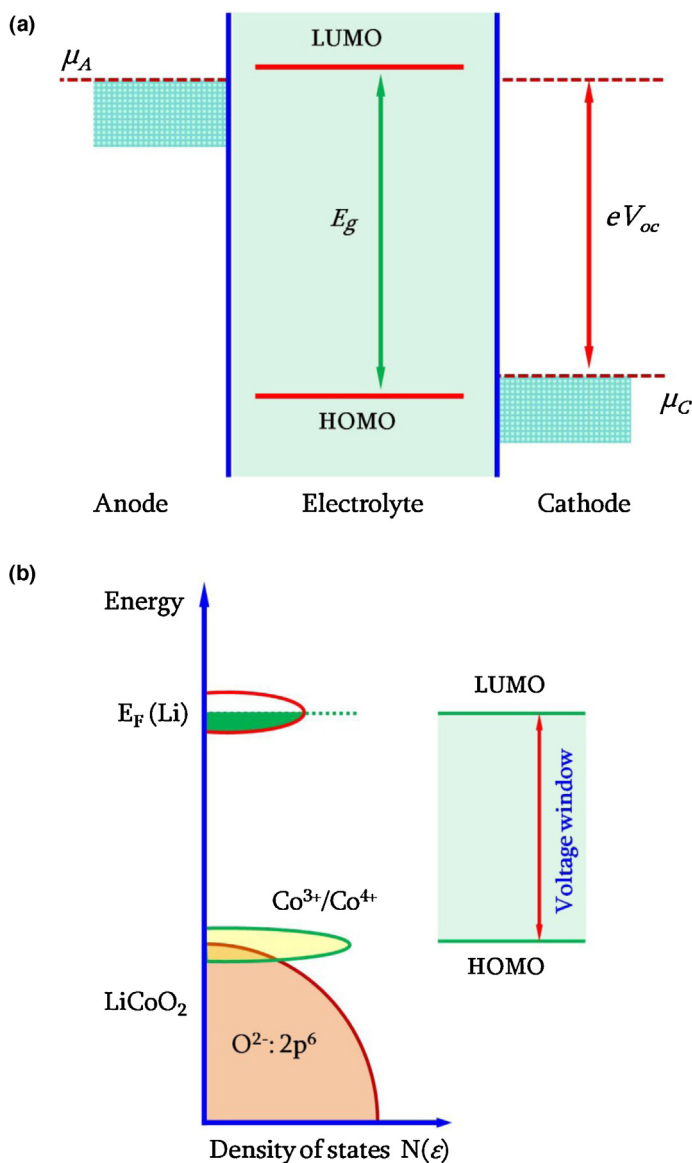
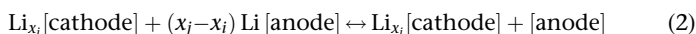


FIGURE 3

(a) Relative energies of the electrolyte window, E_g , and the relationship between electrochemical potentials of electrodes and the HOMO or LUMO of the electrolyte [2]. (b) Schematic energy diagram of the electrochemical potentials of lithium metal and LiCoO_2 and their relative energy positions with respect to the HOMO and LUMO of the liquid electrolyte [31].

(O_2) when the top of the anion p-band is located above the energy state of transition metal ions (e.g., $\text{Co}^{3+}/\text{Co}^{4+}$) [31,74], as illustrated in Fig. 3b. During the charge/discharge processes, the lithium insertion and extraction can be generally described using the following reaction:



where x_i and x_j indicate the solid solubility limits of the intercalation reaction. The difference in Gibbs free energy (ΔG) for the reaction between the charged state and discharge state is described by the following equation [26]:

$$\Delta G_r = \Delta H_r - T\Delta S_r = \Delta U_r + P\Delta V_r - T\Delta S_r \quad (3)$$

where P is the pressure and T is the temperature of the system. The terms $P\Delta V_r$ and $T\Delta S_r$ correspond to the volume change and the

change in the vibrational and configurational entropies of ion insertion or extraction, which are negligible as they are of the order of 10^{-5} and 10^{-2} eV, respectively. ΔU_r is the change in internal energy, which can be approximated as 2–3 eV to evaluate ΔG_r in the reaction [26,49,75]. The chemical potential μ is correlated with the partial molar quantity of Gibbs free energy G [76]. Thus, the equilibrium voltage, $E(x)$, can be obtained by combining equations (1) and (3), as follows:

$$E(x) = \frac{-\Delta G}{(x_j - x_i)F} \quad (4)$$

where F is the Faraday constant. Islam and Fisher computationally investigated the cell voltage derived from the change in Gibbs free energy of ion insertion [50].

Potential hysteresis

Hysteresis is always observed between the charge and discharge curves in all charge/discharge measurements of electrode materials, which can be explained in two ways. First, Goodenough et al. consider the charge potential to be greater than the discharge potential (Fig. 4a) due to the polarization arising from the internal resistance of the electrode materials [31]. This polarization decreases the discharge potential below the open circuit voltage, and it increases the charge potential to reverse the chemical reaction on the electrode. In addition, the internal resistance drop (IR drop) also leads to a drop in potential (drop in IR) between the end of charge and the beginning of discharge (Fig. 4b). Second, overpotential is the driving force behind electrochemical phase transitions in insertion electrodes [77]. The plateau on the potential–capacity curve indicates the two-phase coexistence region of the phase transition, and the span of the plateau represents the width of the miscibility gap. In general, phase transitions during the charge step are accompanied by the extraction of Li ions from the host lattice and the dragging of electrons from the d orbitals of transition metal ions. Likewise, Li ions and electrons are inserted into the relative lattice positions and electronic orbitals during discharge. It is worth noting that the corresponding energy changes are different in this reversible phase transition. During the discharge step, Li ions enter the interstitial space of the host lattice and electrons are accepted into the transition metal d orbital, followed by an energy decrease and phase stabilization. However, in reverse, more energy is consumed as ions and electrons must be promoted from the lower energy states. In particular, the energy spent during charge is slightly higher than that delivered during discharge. This energy difference is the source of the potential gap between the charge and discharge curves. Thus, a higher overpotential results in a phase transition at the electrode during the charge procedure. The IR drop originates from the change of internal resistance, including the resistance of the electrolyte, electrode materials, and other connectors or auxiliaries. The drawback of the IR drop includes energy consumption, leading to a decrease in the efficiency of the battery and the safety issues from the released heat. These resistances can be decreased or eliminated to overcome the side effects efficiently. Effective approaches used in laboratories or factories include a conductive coating on the surface of active materials [57], which enhances the performance of the connecting components and makes use of the highly conductive auxiliaries.

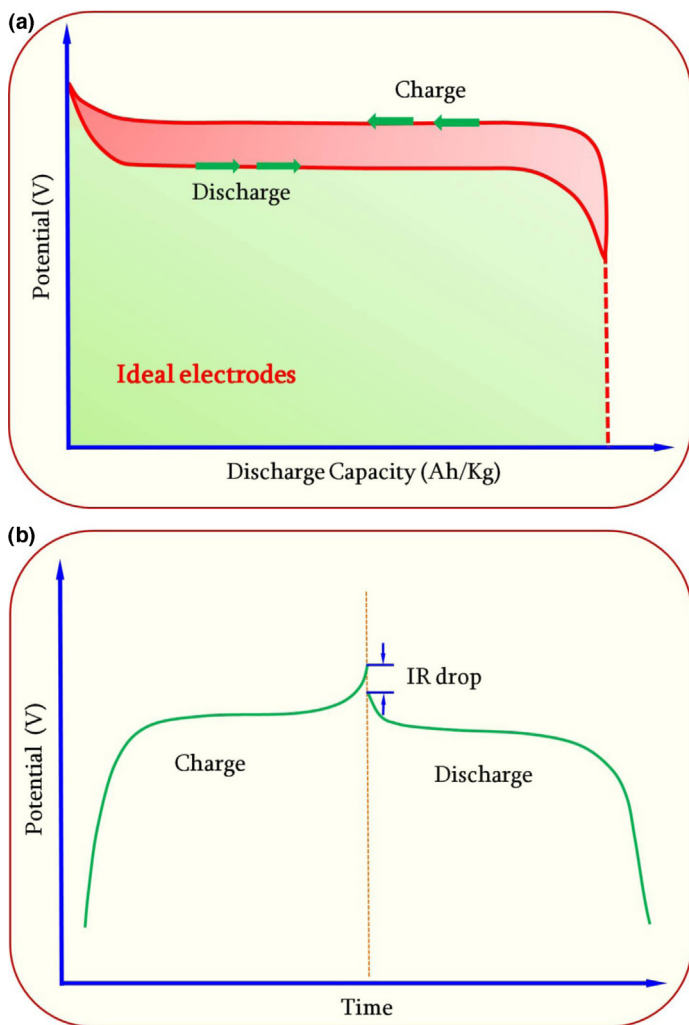


FIGURE 4

(a) Schematic of potential hysteresis in the charge/discharge procedure of an ideal insertion electrode material. This electrochemical potential is caused by the energy difference of phase transitions between the charge and discharge procedures. (b) Illustration of the potential drop in the interval between charge and discharge. Internal resistances chiefly induce the IR drop, which in turn gives rise to side effects that lead to safety issues.

Criteria of element selection for electrode materials

Several selection criteria of electrode materials for lithium-ion batteries are proposed, including societal, economical, and technical considerations. These include their natural abundance; lack of competition with other industrial applications; eco-friendly nature for processing, usage and recycle; and low cost. Technologically, the electrode materials must offer a large reversible storage capacity at the desired electrochemical potential.

The theoretical capacity of electrode materials corresponds to the number of reactive electrons and the molar weight of the designed materials, as expressed by the following equation [79]:

$$C_t = \frac{nF}{3.6 \times M} \quad (5)$$

where n is the number of reactive electrons per formula unit, M is the molar weight of materials, and F is the Faraday constant. The number of electrons is correlated with the number of Li ions accommodated in the host lattice. The equation implies that

smaller molecular weight and accommodation of more electrons per formula unit can produce a higher capacity in theory. For example, the metal lithium anode has a theoretical capacity of 3850 mAh/g and silicon reaches a value up to 4200 mAh/g if the alloying compound is $\text{Li}_{22}\text{Si}_4$ [37,80]. In the series of cathodes, LiCoO_2 possesses a theoretical capacity of 273mAh/g if one Li ion is inserted into the layers of the host and V_2O_5 has a higher capacity of 443 mAh/g when three Li ions are inserted into the host lattice [48,81]. However, in practice, a capacity of 140 mAh/g is obtained as only half of the Li ions can be reversibly inserted into or extracted from the LiCoO_2 host [82]. Nevertheless, lighter elements are favored as electrode materials for their higher specific capacities, as are most elements in the first four periods of the periodic table. The advantages of transition metal oxides as cathode materials are incomparable, as their variable valence states facilitate more electron-storing sites. Furthermore, the electronegativity and ionization energies determine the types of bonds between transition metal ions and ligands [78]. The available and potential elements for use as electrode materials are marked by different colors in Fig. 5. It is to be noted that some elements were verified as having considerable electrochemical performance in the recent literature, such as Nb [83] and Sn [38,84], although they were excluded in this colored table.

Electronegativity is an essential factor that affects the electrochemical potential of electrodes [78]. Electronegativity describes the tendency of an atom or a functional group to attract electrons (or electron density) toward itself. This property intensifies with increasing atomic number in the same row. The difference in electronegativity will determine the character of chemical bonds formed between transition metal ions and anions or anionic ligands. A larger difference in electronegativity predicts the formation of a more ionic bond, whereas smaller differences denote a more covalent bond. Materials with more ionic bonds typically form dense structures, whereas those with more covalent bonds form a poorly packed structure. The structure density not only influences the crystal or phase stability of materials but also affects the specific site energy of Li ions, which is correlated with the electrochemical potential of materials.

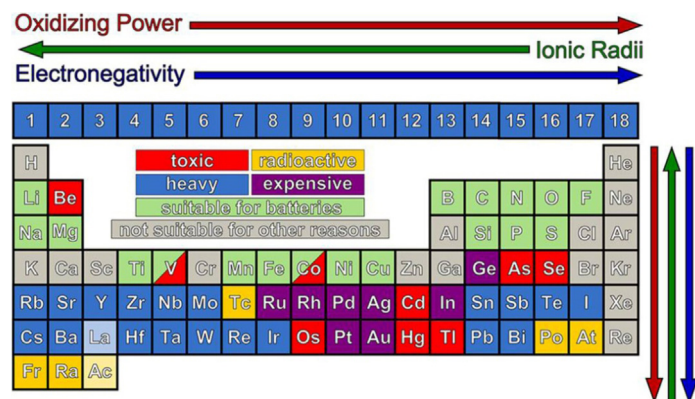


FIGURE 5

Elements available for the design of new electrode materials. The colored quadrates are excluded due to their low capacity, high cost, toxicity, or radioactivity. Note that, despite their toxicity, some transition metals, such as V and Co, are still actively investigated [78]. This colored table can be revised as some materials display acceptable electrochemical performance in recent reports, such as Sn, Nb, Mo, and W.

Cathode materials are commonly transition metal compounds, oxides, or complex oxides. Such transition metal compounds have layered, spinel, or olivine crystal structures, and transition metal cations typically display four- and/or sixfold coordination with oxygen anions, anionic clusters, or ligands. Lithium ions are inserted via an electrochemical intercalation reaction. While lithium ions occupy the space between adjacent layers or unoccupied octahedral or tetrahedral sites, an equal number of electrons enter the available d orbitals of the transition metal cations in the host crystal. The change in Gibbs free energy and the electrochemical potential of the electrode are markedly dependent on the valence state, ionic radius, electronegativity, and the local environment of the cations in compounds. Figure 6 shows the increase in the electrochemical potential of cathodes with the number of electrons in d orbitals of transition metal elements of the same period. This observation can be easily explained as follows: Given the transition metal ions show the same coordination and valence, the ionic radius of the transition metal cations in the same row would decrease with increasing atomic number, as the electrons in the outer shell are more strongly attracted by atomic nuclei, resulting in higher energy consumption or release during electron transfer. Similarly, if the period increases in the same family, the binding energy of electrons and the electrochemical potentials of cathodes decrease, as the nuclei not as strongly attracted to the $4d$ electrons as they are to the $3d$ electrons [49]. As weaker attraction corresponds to a lower energy for electron transfer, the corresponding materials have a lower potential. The more energy released when electrons are inserted into orbitals, or the more energy consumed when electrons are promoted from orbitals, the higher the electrochemical potential of the electrode materials. This can be well described by the following equation [49]:

$$-\Delta G = nFE \quad (6)$$

where ΔG denotes the change in internal energy during the ion and electron insertion or extraction with a dominant effect arising from ions, n is the number of electrons stored in the formula unit, F is the Faraday constant, and E is the displayed electrochemical potential of the electrode materials. Thus, the interaction between

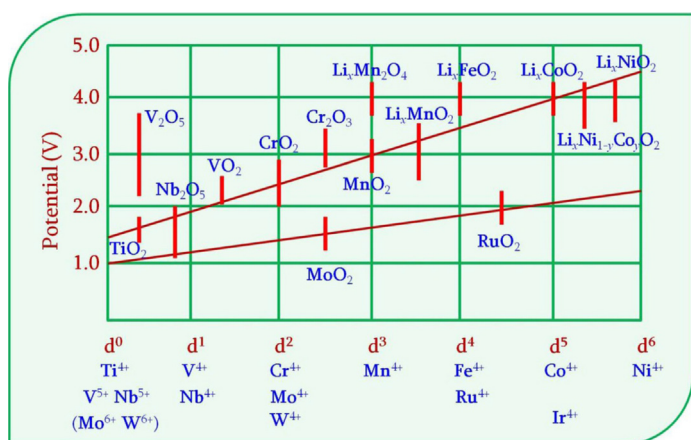


FIGURE 6

The voltage range of compounds consisting of transition metal ions [49]. This schematic exhibits the relationship between electrode potential and the number of electrons in the d orbitals of transition metal ions; in general, the potential increases with increasing number of electrons in the d orbitals.

atoms or electrons affects the change in internal energy of the reaction, leading to a different electrochemical potential.

The selection of center cations was discussed given that oxygen ions are the coordinating ligands to consider the energy for electron transfer. In fact, ligands with different elements and/or configurations possess varying electronegativity because of the internal interactions of the ligand components with different electronic states. The presence of polyanionic groups with greater electronegativity that replace oxygen ions in the framework of electrode crystals would lead to more ionic bonds between metal ions and oxygen ions (M–O bonds). This enhanced ionic character reduces the separation between the bonding and antibonding orbitals, which results in a decrease of the lowest unoccupied M-3d orbitals, that is, an increased electrochemical potential [78]. Electrode materials with polyanionic groups as building groups, such as phosphates, silicates and sulfates, have higher electrochemical potential than the corresponding transition metal oxides containing lithium ions [85]. For example, LiCoPO₄ possesses a high electrochemical potential of 4.8 V, whereas LiCoO₂ has a potential of approximately 4 V. Figure 7a presents the average electrochemical potentials and storage capacities of the transition metal phosphates [86]. Both the gravimetric capacities and electrochemical potentials agree well with the abovementioned principle. Bismuth (Bi), belonging to period VI and group V of the periodic table, has a large atomic number and large electronegativity, which leads to a higher electrochemical potential but a smaller gravimetric capacity than molybdenum (Mo), which has low electronegativity and relatively small atomic weight. With respect to the transition elements of period IV, the electrochemical potentials of phosphates increase with increasing atomic number (marked by the green dash rectangles), which also follow the same electronegativity rule. However, as an exception, Mn phosphate has a higher electrochemical potential than Fe phosphate, despite the stronger electronegativity of Fe. This abnormal phenomenon originates from the electron configuration in the $3d$ orbitals of Fe²⁺ and Mn²⁺ in the ligand field, the details of which are discussed in the section ‘Regulating Electronic Structure.’ For a specific transition metal cation, different polyanionic groups will result in different electrochemical potentials for the Li-ion intercalation. Again, this following the same electronegativity rule, that is, the greater the electronegativity of the polyanionic group, the higher the electrochemical potential. Figure 7b compares the electrochemical potentials of iron polyanionic compounds, with a significant increase in electrochemical potentials being observed with increasing electronegativity of polyanionic groups [85]. In addition, it should be noted that, at a given potential, polyanions have better thermal stability than their oxide counterparts do [87]. Studies have found that an inductive effect alters the ionic-covalent nature of bonds in polyanionic compounds compared with oxides [78,88]. In transition metal polyanion compounds, the counterions (X = Mo, W, S, P, Si) share the corner oxygen with the transition metal cations in the M–O–X linkages; thus, through an inductive effect, the counterions markedly influence the strength of the M–O covalency [87,88]. The inductive effect pulls some charge density out of M–X bonds to decrease their orbital overlap, increasing the ionic character of the bonds. Similarly, fluorides possess higher electrochemical potential than polyanionic compounds due to the strongly inductive effect of fluorine

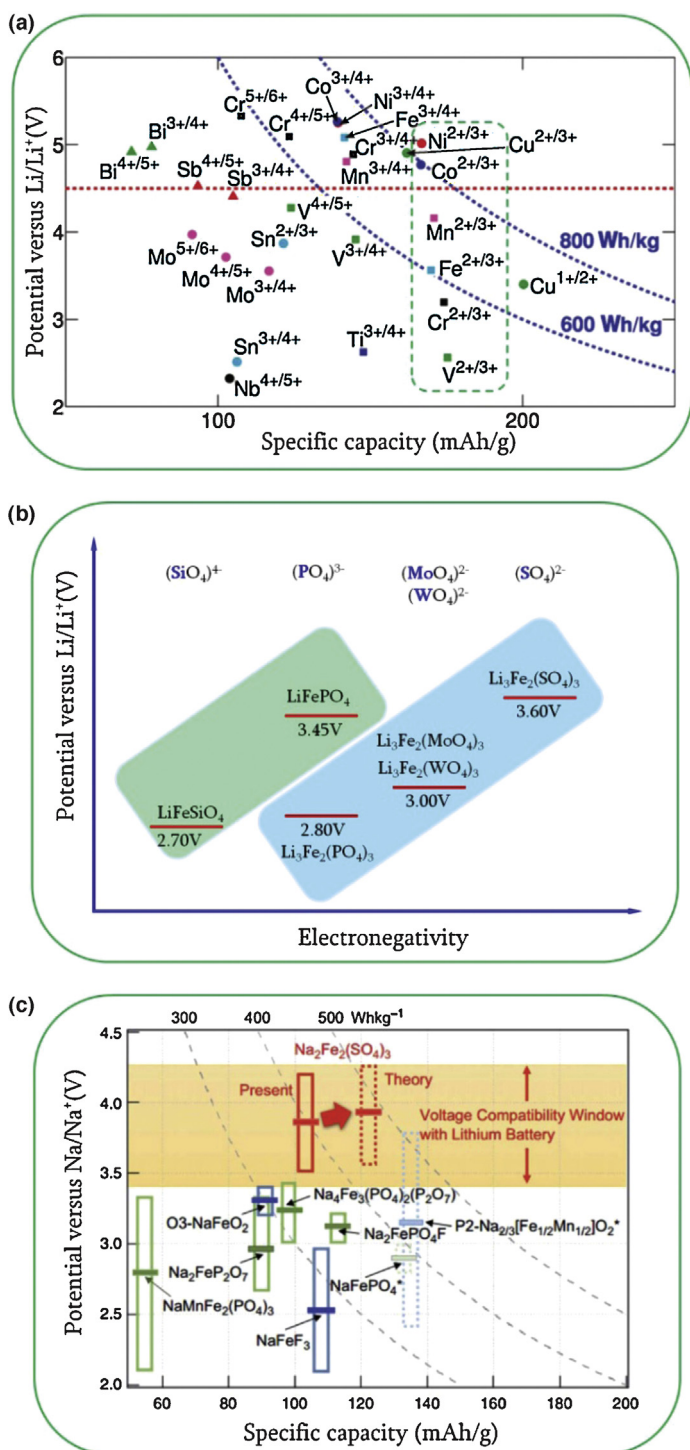


FIGURE 7

(a) Average potential in phosphates versus maximum gravimetric capacity achievable. Energy density curves at 600 and 800 Wh/kg are drawn in the figure (blue dashed lines). The red dashed line indicated the upper potential, which is considered safe against the decomposition of the normal electrolyte. Different colors and markers are used to distinguish different elements [86]. The green dashed rectangle shows the potential tendency of phosphates in the third period. (b) The relationship between average potential of Fe-based materials and electronegativity of polyanionic groups. The potentials increase with increasing electronegativity of polyanionic groups. Data on the average potentials of materials were collected from the literature [85]. (c) Comparison of the Fe-based cathode materials in the Na-ion battery system. The potentials of the cathodes follow the electronegativity rule for selecting elements or anions [91].

anions [33,78,89,90]. Compared with Li-ion electrodes, sulfates are used as cathodes to obtain a higher potential than phosphates in Na-ion batteries (Fig. 7c) [91]. The stronger X–O bonds would decrease the orbital overlap of the M–O bonds, increasing the ionic character of the M–O bonds and the electrochemical potential.

Therefore, selecting elements is the first step wherein the atomic weight, abundance, environmental impact, and cost are to be considered. The electronegativity of the elements and the counterions is another key parameter that determines the electrochemical potential of the electrode materials.

The effects of structures on electrochemical potential of electrodes

For a material with a given chemical composition, its chemical, electrochemical, and physical properties are significantly influenced by its microstructure, crystal structure, and electronic structure. The electrochemical properties of electrodes are determined by the intrinsic nature of the selected materials; however, their microstructures may vary greatly with the synthesis or processing methods and conditions. For instance, working ions are inserted into the host lattice along certain crystallographical orientations; thus, exposing the entrance of these orientations enhances the ion transportation and the rate capability [92]. Although the crystal structure is an inherent property of a certain material, the crystal parameters can be slightly modified by introducing dopants. Introduction of Ni^{2+} to V_2O_5 resulted in enhanced cyclic stability and specific capacity simultaneously. Introducing dopant atoms or vacancies can significantly affect [93] the crystal field, thus tuning the electronic structure in transition metal compounds and adjusting the electrochemical potential [72].

Designing microstructure

In the past decades, several studies have synthesized and characterized various nanostructured materials for use as lithium-ion battery electrodes; these nanomaterials have been shown to enhance the electrochemical properties considerably [94]. These extensive studies have illustrated the benefits of nanomaterials as follows: (i) the enhancement of the reversibility of lithium-ion insertion and extraction reaction in nanostructured electrodes without destroying the crystal structure, which would be difficult, if not impossible, in micrometer-sized particles, such as $\beta\text{-MnO}_2$ [95]; (ii) the reduction in the diffusion or transport distance of the Li ions and electrons accompanying the Li-ion insertion and extraction reactions; and (iii) the change in the site energy of Li ions occupying the host lattice, which affects the electrochemical potential of the electrodes. LiCoO_2 , a widely commercialized cathode material used in Li-ion batteries, possesses an electrochemical potential or a discharge plateau at 3.9 V (vs. Li/Li^+) with micrometer-sized particles. However, the discharge potential plateau disappeared with the reduction in the size of LiCoO_2 particles to 6 nm [96] (Fig. 8a). This effect can be summarized on three levels: microstructure, crystalline structure, and electronic structure. On the microstructure level, the reduced particle size shortened the path of Li-ion transfer, thus drastically increasing the rate capability, as shown in the original text as well as other reports [97]. Small-sized particles have a large specific surface area and therefore a high surface energy. The bond length of Co–O in the crystal structure increases with the decrease in particle size. The

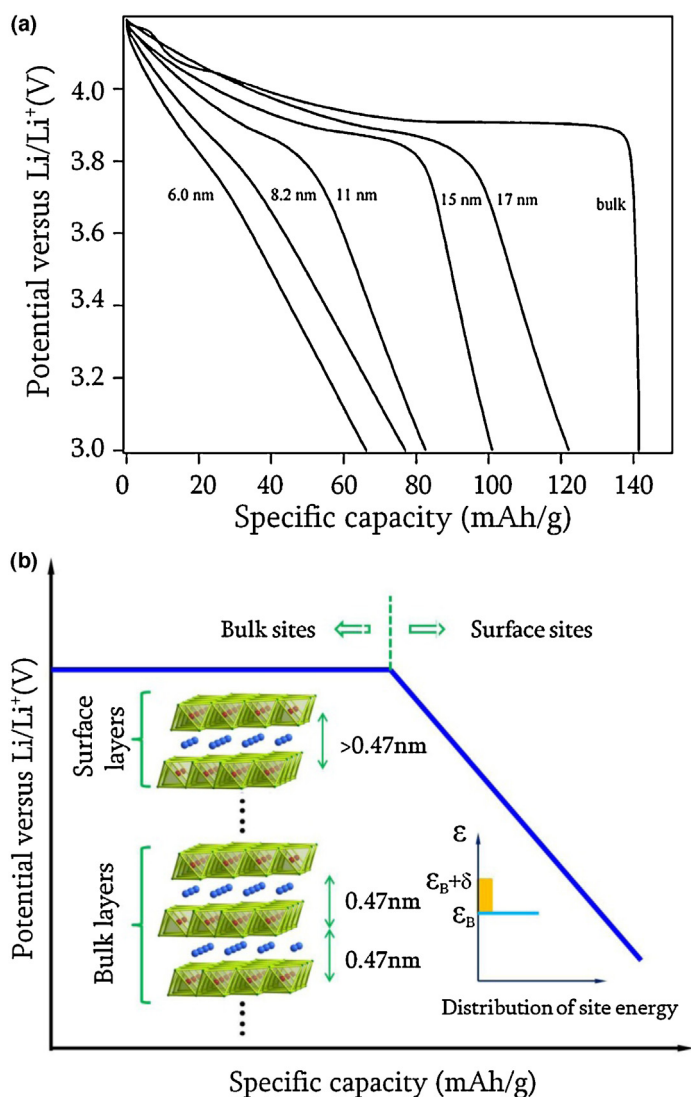


FIGURE 8

(a) The profiles of discharge curves of LiCoO_2 with different particle sizes. Capacitor behavior becomes more dominant with decreasing crystallite size, accompanied by steeper sloping potential profiles. (b) Expected discharge potential curve for nanocrystalline LiCoO_2 . Capacitor behavior is expected for the intercalation of Li ions into the surface layers. The capacitor behavior becomes stronger with increasing number of surface layers and decreasing crystallite size. More importantly, site energy on the surface fluctuates and exceeds that of the internal bulk, and the external energy needed for ion transfer decreases, leading to reduced potential plateaus [96].

interaction between atoms weakens not only due to the reduction of the electrostatic forces but also from the antibonding character of the electron occupying the e_g orbital [96]. The site energy related to Li-ion insertion also increases, causing a synchronous decrease in the energy difference before and after Li-ion insertion. Thus, the potential plateau declines and disappears gradually. On the electronic level, Co (II) ions appeared on the surface of nanoparticles. Electrons in Co (II) have a high spin state of $t_{2g}^5 e_g^2$, but Co (III) in bulk LiCoO_2 have a low spin state of $t_{2g}^6 e_g^0$ [96]. Figure 8b illustrates the expected discharge profile of nanocrystalline LiCoO_2 . The intercalation of Li ions into the surface layers leads to a capacitor behavior. As the quantity of surface layers increased with decreasing crystallite size, the capacitor behavior becomes

stronger with decreasing crystallite size [96]. The site energy also fluctuates and increases on the surface with reduced particle sizes, resulting in a sloping discharge potential profile. The destruction of the crystal lattice and enlargement of the surface area enhanced the capacitor behavior, but it decreased the specific capacity as the internal sites were destroyed compared with those of micro-sized LiCoO_2 .

Crystal structure

The crystal structure represents the unique arrangement of atoms that forms symmetric patterns. Atoms occupy positions that minimize the total energy in a given crystal structure, just as electrode materials do in rechargeable batteries. Phase transitions are observed in the electrode materials, and the change in Gibbs free energy determines the electrochemical potentials of materials during the process of ion insertion or extraction. The insertion or extraction of lithium ions in electrode materials via electrochemical intercalation involves two simultaneous processes: (1) the addition or removal of lithium cations to or from the host crystal lattice and (2) the addition or subtraction of an equal number of electrons to the d orbitals of the transition metal cations in the host crystals. The electrochemical potential of the electrode material is directly correlated with the energy required to add or remove lithium ions to the host crystal lattice and to reduce or oxidize the transition metal cations in the host crystal. Li ions occupy the tetrahedral and/or octahedral sites in intercalation electrode materials. Although both LiO_4 ($r_{\text{Li}}/R_{\text{O}} = 0.415 \gg 0.225$) and LiO_6 ($r_{\text{Li}}/R_{\text{O}} = 0.535 \gg 0.414$) are stable [98], the LiO_4 tetrahedron is much smaller than the LiO_6 octahedron, and the insertion and extraction of Li-ions to and from oxygen tetrahedrons and oxygen octahedrons result in different changes in the Gibbs free energy, as indicated by the different electrochemical potentials. For example, in the spinel crystal $\text{Li}_x\text{Mn}_2\text{O}_4$, Li ions are inserted into the tetrahedral sites (at $x \leq 1$) and octahedral sites (at $x \geq 1$) at distinctive electrochemical potentials: 4.3 V relative to Li/Li^+ for the insertion of Li ions into smaller oxygen tetrahedrons and 3.1 V for Li ions to be inserted into larger oxygen octahedrons [22]. In addition, the introduction of defects and disorder of atomic arrangement can also modify the discharge potential of electrode materials by changing the site energy or local atomic environment of working ions.

(i) Site energy

The Gibbs free energy is used to estimate the equilibrium potential of electrode materials. Site energy, the main component of the Gibbs free energy, is defined as the contribution of the enthalpy change (H) to the process of ion intercalation. It is described as dH/dn (n is the number of intercalated Li atoms), which comprises a part of the chemical potential [99]. The lower the site energy in a crystal lattice, the more external energy is consumed to transfer one ion from the occupied site to a free state. Different positions possess different site energies and produce different potentials when ions are inserted into or extracted from host materials. Spinel, olivine, and layer structures are three common crystal structures in the intercalation cathodes of rechargeable batteries. Spinel $\text{LiNi}_{0.5}\text{Mn}_{1.5}\text{O}_4$ and olivine LiFePO_4 show flat potential plateaus [47,100], but layered LiCoO_2 and $\text{LiNi}_{1/3}\text{Mn}_{1/3}\text{Co}_{1/3}\text{O}_2$ display sloping potential profiles [45] (Fig. 9). This distinct difference arises from

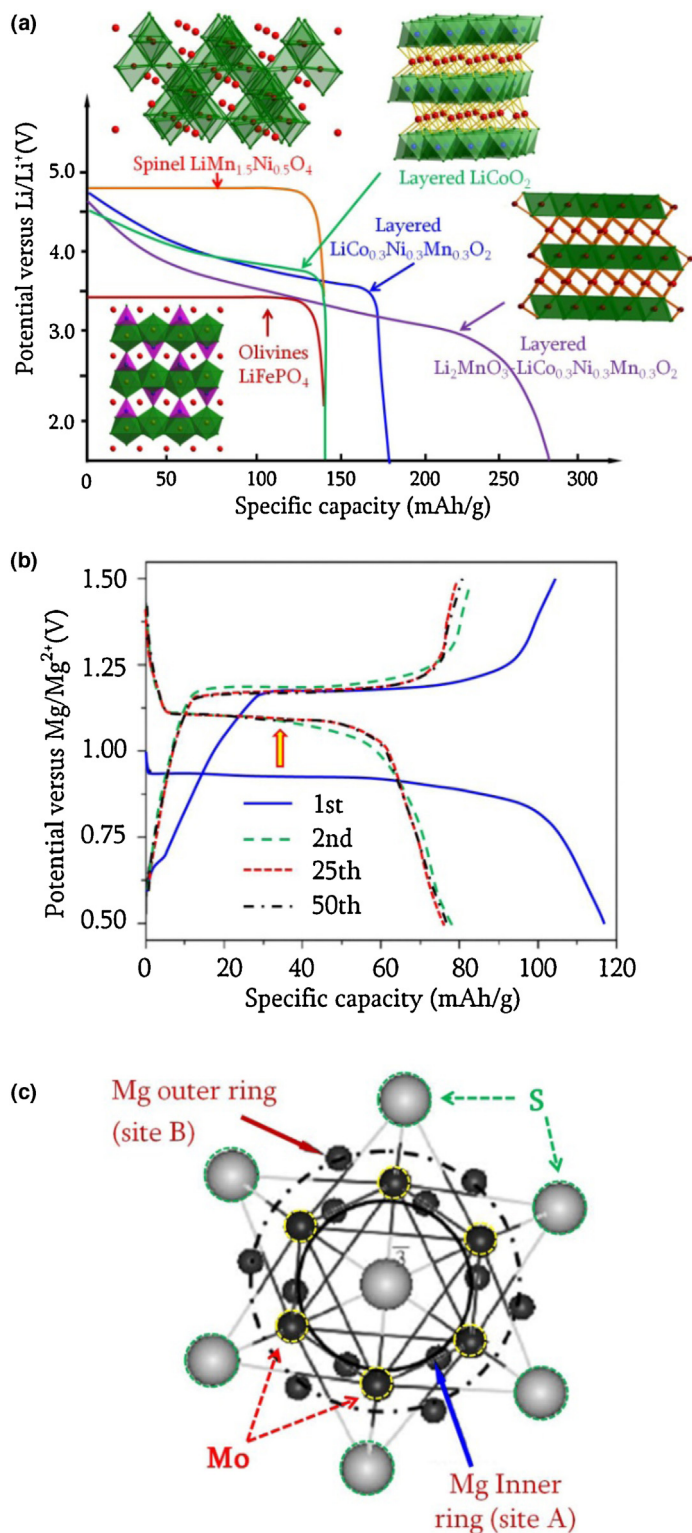


FIGURE 9

Li-ion battery cathodes: important formulae, structures, and potential profiles during discharge [33,100]. (b) Charge–discharge potential profiles (first, second, 25th, and 50th cycle) of the electrode comprising Mo_6S_8 at a constant current rate of 20 mA/g within the potential range of 0.5–1.5 V. Mg metal was used as reference electrode [111]. (c) Basic crystal structure of the $\text{Mg}_x\text{Mo}_6\text{S}_8$ ($0 < x < 2$) cathodes, with 12 potential sites for storing Mg^{2+} . These positions can be divided into two sets, the inner and outer rings [112].

their unique crystal structures. Each spinel unit cell consists of eight molecules of AB_2O_4 ; 32 oxygen anions form a close-packed cubic oxygen anion lattice with 32 large octahedral and 64 small tetrahedral sites. In a normal spinel structure, B cations occupy half of the octahedral sites, whereas A cations occupy one-eighth of the tetrahedral sites. The olivine structure consists of vertex-sharing MO_6 octahedrons, as well as PO_4 tetrahedrons that share one edge and all vertices with MO_6 octahedrons. In LiFePO_4 , oxygen anions form a close-packed array, with half of the octahedral sites being occupied by lithium or iron ions and one-eighth of the tetrahedral sites by phosphorus ions. However, LiMO_2 layer-structured oxides possess an O3-type crystal structure, with the oxygen anion planes being stacked in an ABCABC sequence. In the oxygen anion planes, each MO_6 octahedron shares four edges with others. If there are n number of oxygen anions in a unit cell, oxygen anions would form $2n$ tetrahedral and n octahedral sites [49]. As an example, layered LiCoO_2 has four tetrahedral and two octahedral sites [101], with both the Li and cobalt ions occupying the octahedral sites. The lithium layers lie between slabs of octahedrons formed by cobalt and oxygen ions [102].

In both spinel and olivine crystals, oxygen anions form a robust framework of a closely packed anion sublattice with a densely packed atomic arrangement in three dimensions (3D), whereas layer-structured crystals consist of relatively loose stacks perpendicular to the two dimensional planes. When subjected to the insertion or extraction of lithium ions, the robust 3D frameworks of spinel or olivine crystal electrodes show negligible structural distortion, retaining the same site energy and displaying an almost constant electrochemical potential. However, the layered structures are distorted to a larger extent than are spinel and olivine crystals, leading to a slight increase in site energy and a sloping potential profile for lithium-ion insertion into layered structures. For example, Li^+ in layered Li_xMnO_2 will only occupy the octahedral sites for all $0 < x < 1$ compositions, whereas the Li^+ of spinel $\text{Li}_{2x}\text{Mn}_2\text{O}_4$ oxides occupy all tetrahedral sites at $0 < x < 0.5$ and all octahedral sites at $0.5 < x < 1$ [31]. The different positions occupied have different site energies that display different potential profiles and different average potentials, as shown in Fig. 9a. It is worth noting that the electrochemical charge–discharge process in cycled LiMnO_2 results in not only the partial oxidation of the manganese ion but also the migration of Mn into the interlayer lithium site, such that the layered spinel structures coexist [103]. The lattice instability of layered manganese oxide for Li-ion insertion is responsible for the formation of two plateaus at around the 3- and 4-V regions after the first electrochemical cycle [103,104]. The 3-V plateau is similar to that of spinel $\text{Li}_{2x}\text{Mn}_2\text{O}_4$ ($0.5 < x < 1$) for the phase transition in LiMnO_2 from the layered to spinel structure, which possesses the same storing sites for Li ions. However, the potential profiles of 3 and 4 V differ for layered LiMnO_2 and spinel LiMn_2O_4 , with a sloping potential profile in the former [105], but a flat plateau in the latter [49]. This difference is caused by the presence of storing sites at the 16c octahedron in the former and the 8a tetrahedron in the latter. The Li ions located at 16c octahedrons experience stronger repulsive forces from the local environment, with a resulting increase in site energy and a lower potential. The weaker repulsions at the 8a sites, however, lead to a lower site energy and a corresponding higher potential. These are in agreement with the predicted data, as shown in

Fig. 9a. Olivine LiFePO_4 differs from spinel derivations in the PO_4 tetrahedrons with FeO_6 octahedrons, which support the two-dimensional (2D) planes and form a robust 3D framework (shown in inset of Fig. 9a). These are similar to the spinel LiMn_2O_4 , MnO_6 octahedrons that link the 2D planes of MnO_6 octahedrons to build the 3D framework. Li ions occupy the remaining octahedral sites with equivalent site energy, leading to an expected potential plateau, as shown in Fig. 9a. For example, Li ions extracted from the host of LiFePO_4 can induce the expansion along the c axis by 1.94% [106] and the shrinkage along a and b by 4.98% and 3.62%, respectively, when the phase transforms to FePO_4 , but the corresponding expansion change in LiCoO_2 is 2.56% in the c axis and 0.35% along the a axis [107]. The lattice change perpendicular to the c axis is smaller in olivine LiFePO_4 than in layered LiCoO_2 during Li-ion insertion or extraction, maintaining a constant site energy that leads to a potential plateau. Spinel $\text{Li}_4\text{Ti}_5\text{O}_{12}$ can be used as an intercalated anode because of its robust 3D framework and equivalent storage sites for Li ions, and thus displays a similar stable voltage plateau [108] to that for LiMn_2O_4 cathode. Apart from these ordered crystalline materials, disordered rock-salt materials have been increasingly studied at present [109,110]. These novel materials displayed sloping charge/discharge potential profiles, which arise from the nonequivalent site energy due to the disordered cations in the crystal lattices. This phenomenon is also observed in amorphous materials, as discussed in a subsequent section.

An exceptional trend of the discharge potential curve was observed in the Mo_6S_8 cathode of the Mg-ion battery (Fig. 9b). In the first discharge cycle, the discharge potential plateau is located at 0.92 V, but it increased to 1.10 V in the following cycles. A differential capacity versus potential curve was used to analyze the origin of this difference. The initial Mg^{2+} insertion into Mo_6S_8 may have been kinetically limited and thus intrinsically very slow at the rate used currently. Therefore, a small overpotential of ~ 200 mV from the equilibrium magnesiation potential of ~ 1.10 V was required [111]. In addition, the local atomic environment of the crystal structure changed in the first two cycles. The crystal structure of $\text{Mg}_x\text{Mo}_6\text{S}_8$ consists of a stack of Mo_6S_8 clusters and 12 available lattice sites that allow Mg^{2+} insertion in a 3D framework. These 12 lattice sites form two sets of rings. The first ring, also called the inner sites, has a six-fold symmetry of lattice positions (Mg A-sites) close to the unit-cell origin. The second ring also has a six-fold symmetry (Mg B-sites), which forms the outer sites, located around the inner positions [112] (Fig. 9c). The insertion of Mg^{2+} into the crystal lattice can stabilize the Mo_6 structure by modifying the distances between the Mo atoms, due to charge transfer from the Mg^{2+} to the Mo or S atoms. In the initial magnesiation stage, all the 12 sites are occupied by the Mg^{2+} ions. However, in the following demagnesiation stage, only Mg^{2+} from the outer rings (one Mg^{2+} per Mo_6S_8 unit) can be extracted due to the strong repulsive forces between the rings. As a result, some of the Mg^{2+} ions move circularly between the inner sites and are trapped in the Mo_6S_8 host, which does not allow their reversible cycling through the host CP lattice. The trapped Mg ions play a role in the chain linking of the Mo_6S_8 clusters, due to the strong interaction between Mg and S ions. However, the trapping effect is not seen in the selenide host [113], indicating that the stronger electronegativity of Se influences the interaction between Mg and

Se ions in the crystal structure. The stronger interaction between S and Mg ions decreases the distances of Mo_6S_8 clusters, leading to a decrease in the site energy of the outer ring and a higher discharge potential after the initial discharge. Thus, site energy is an essential and adjustable factor for modifying or designing materials with an expected discharge potential plateau.

(ii) Defect effects

Although site energy is the main determinant of the potential plateaus of electrodes, defects are also a factor affecting the electrochemical potential of electrodes. These can be introduced through doping [93], atmosphere treatment [114,115], and control of synthesis methods [116,117]. Alien atoms replace the inherent atoms in the host to produce cation or anion vacancies, which in turn affect the electrochemical performance of the electrode due to the modified chemical pressure, lattice distortion or change in crystal field.

Doping of Ni^{2+} -substituted partial V^{5+} into the V_2O_5 matrix can effectively increase the average potential and specific capacity of the electrode, compared with undoped V_2O_5 (Fig. 10) [93]. First, low-valence Ni ions introduced into the crystal structure of host V_2O_5 can produce a certain amount of oxygen vacancies to maintain the electroneutrality. The lower-valence Ni in place of high-valence V can effectively decrease the electrostatic repulsion between the cations, thus decreasing the Li site energy and increasing the potential of doped materials. More importantly, the introduced oxygen vacancies can play a role in the nucleation for phase transitions [115], which benefits the rate capability of electrode materials. Second, Ni^{2+} has a large ionic radius (83 pm) than V^{5+} (68 pm), which may result in local lattice distortion. The larger ions can expand the crystal lattice and increase the bond lengths, reducing the interaction between cations and anions. Thus, the site energy for Li ions decreases with a resulting higher potential, as shown in Fig. 10. Lower-valence cations introduce anion vacancies into the host lattice, but higher-valence cations

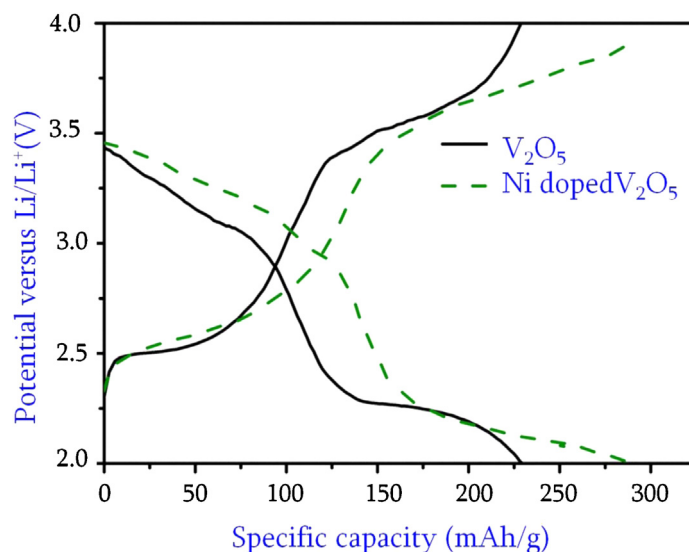


FIGURE 10

Galvanostatic discharge curves of nickel (II)-doped V_2O_5 and undoped V_2O_5 . Ni^{2+} -doped V_2O_5 has a higher average potential and larger specific capacity than undoped V_2O_5 . Defects introduced by low-valence Ni^{2+} plays a key role in enhancing the comprehensive performance [93].

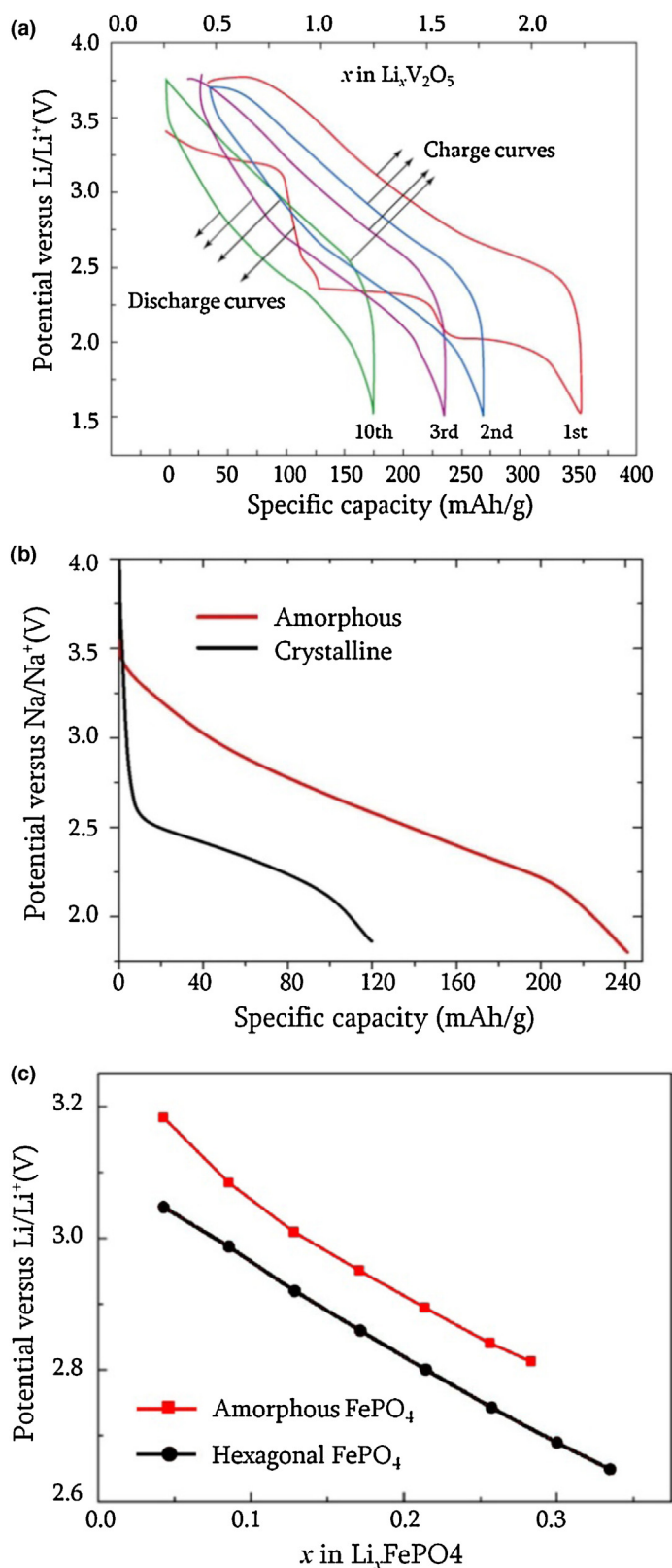


FIGURE 11

(a) Charge/discharge curves of nanowire V_2O_5 at a current density of $C/20$ in the voltage range of 1.5–3.75 V [49]. The initial discharge curve exhibits four plateaus, but all disappear in the following cycles. The crystal structure undergoes a slight adjustment as partial lithium ions occupy the sites irreversibly, leading to electrochemically nonequivalent sites. (b) Discharge curves of crystalline and amorphous V_2O_5 in a sodium battery. Amorphous V_2O_5 possesses a higher average potential and larger specific capacity than

can introduce cation vacancies, which can increase the corresponding charge storage capacity. Benjamin reviewed studies on cation vacancies in electrodes in more detail [118]. It is worth noting that defects effect not only the crystal field but also the discharge potential, which is discussed in detail in the section of electronic structure.

(iii) Amorphous state

Crystalline materials are considered suitable for ion insertion and extraction, because their regular atomic arrangement offers unique spaces for accommodating removable ions. However, an inferior degree of crystallinity has attracted increasing research interest, opening up avenues for developing the electrochemical performance of electrode materials [117,119–122]. Mesoporous amorphous materials are conducive to the full infiltration of the electrolyte, which reduce the migrating distance of Na/Li ions, facilitate Na/Li-ion exchange across the interfaces, and tolerate the large volume change of the electrodes during Na/Li-ion insertion/extraction. These factors greatly enhance the Na/Li-ion storage kinetics and structural stability [119,122]. Recent reports demonstrate the feasibility of using high-performance electrode materials, such as amorphous V_2O_5 [117] and $FePO_4$ [121,122]. Amorphous V_2O_5 enhances not only the capacity and potential of sodium batteries [117] but also the reversibility and rate capability of lithium batteries [120]. Most studies often focus on improving the specific capacity or cycling stability of a certain material, but studies on the factors affecting the electrochemical potential are limited. V_2O_5 has been extensively studied as cathodes in Li-ion batteries, with the basic characteristics being established. In the first discharge curve, four plateaus are displayed because several sites can accommodate ions with different site energies. However, the plateaus disappear in the following cycles (Fig. 11a). This can be explained by the partial Li ions that occupy the lattice irreversibly, which induce a slight structural adjustment and change the inherent site energy. In addition, no splitting occurs in the crystal field as V^{5+} does not contain any electron in the 3d orbitals, resulting in continuous energy changes during electron transfer and a sloping discharge curve (Fig. 11b). Amorphous V_2O_5 or $FePO_4$ are currently known to supply a disordered framework for ion storage. The disordered structure not only provides nonequivalent and ample site space but also eliminates the splitting in the normal crystal field of crystalline materials. Both amorphous V_2O_5 and $FePO_4$ exhibit a higher potential than their crystalline forms do (Fig. 11b,c). The accommodation of electronic carriers becomes increasingly difficult as periodicity is lost, which in turn generates the excess value [123]. Moreover, the lithiation reactions occur over a wide potential range, as the Li^+ storage sites, which have been proposed to be vacancies, void spaces, cluster gaps, or interstitial sites, are electrochemically nonequivalent to each other [41,124]. Anode materials with an amorphous state exhibit similar sloping discharge voltage profiles [120,125] to amorphous cathodes, via the same mechanism as discussed for cathode materials.

crystalline V_2O_5 [117]. (c) Potential vs. Li content in crystalline and amorphous $FePO_4$, accommodating electronic carriers becomes more difficult with the loss of periodicity, which in turn generates the excess value [121].

Regulating electronic structure

Microstructures and crystal structures have a significant effect on the potentials of electrodes through site energy, which in turn depends on the local atomic environment around the potential positions for ion storage. Once the materials are selected, the crystal structure and corresponding site energy are settled. The potential of the material can be modified as defects or amorphism can affect its inherent atomic arrangement. The electronic structure may be a determining factor for the displayed potential profiles of materials. Therefore, the crystal field theory (CFT) must be introduced, a model that describes the breaking of degeneracies of electron orbital states, usually d or f orbitals, due to a static electric field produced by a surrounding charge distribution (anion neighbors) [126]. Subsequently, combined with the molecular orbital theory (MOT), this can lead to a more realistic and complex ligand field theory (LFT). The interaction between transition metal cation centers and ligands in a tetrahedron or octahedron will induce the splitting of d or f orbitals, as the like charges of electrons in the d orbitals and in the ligand repel each other. Thus, the d electrons closer to the ligands will have a higher energy than those further away, which leads to the splitting of the energy of d orbitals. This splitting is affected by the following factors: (i) the nature of the metal ion; (ii) the oxidation state of the metal, with a higher oxidation state leading to a larger splitting; (iii) the arrangement of ligands around the metal ion; and (iv) the nature of the ligands surrounding the metal ion. A stronger effect of the ligands could lead to a greater difference between the high- and low-energy d groups [126]. These rules reasonably explain the potential rise in Ni^{2+} -doped V_2O_5 and its amorphous state. The electronic configuration of Ni^{2+} is described as $t_{2g}^6 e_g^2$. Electrons in the e_g orbitals prefer to participate in the chemical reaction. The small splitting between t_{2g} and e_g generates a lower energy state of the e_g orbital, and the difference in energy can be extended between the Fermi energy of the Li metal and the e_g orbital of Ni^{2+} . Thus, the potential can increase compared with the undoped V_2O_5 . By the same effect, disordered atoms join each other irregularly with no fixed coordination number or structure, resulting in sites with nonequivalent energy and no splitting in the d orbitals. Therefore, the discharge curves exhibit a sloping potential profile in the amorphous state.

Three distinctive discharge plateaus of spinel $\text{Li}_x\text{Mn}_2\text{O}_4$ are observed in Fig. 12a, with the first two, at 4.1 and 4 V, being attributed to the reversible extraction/intercalation of one lithium ion from/into spinel tetrahedral sites. The two-step process is associated with a redistribution of lithium ions occupying the small tetrahedral 8a sites in spinel $\text{Li}_x\text{Mn}_2\text{O}_4$, with Li ions exceeding 0.5 in number but not above 1, or with the discharge capacity ranging from 70 to 140 mAh/g [49]. However, the second lithium ions will enter the large octahedral 16c sites in $\text{Li}_x\text{Mn}_2\text{O}_4$ when the inserted number of lithium ions exceeds 1.0, corresponding to a low discharge potential plateau of 3 V [72]. When the number of lithium ions is less than 1, that is, $x = 0-1$, $\text{Li}_x\text{Mn}_2\text{O}_4$ has a cubic spinel crystal structure that is formed by edge sharing between MnO_6 octahedrons, and corner sharing between LiO_4 tetrahedrons and MnO_6 octahedrons (Fig. 12b). When the number of lithium ions exceeds 1, the cubic spinel undergoes structural adjustment and converts to a tetragonal spinel, which is formed by vertex sharing between MnO_6 octahedrons and LiO_6 octahedrons, and

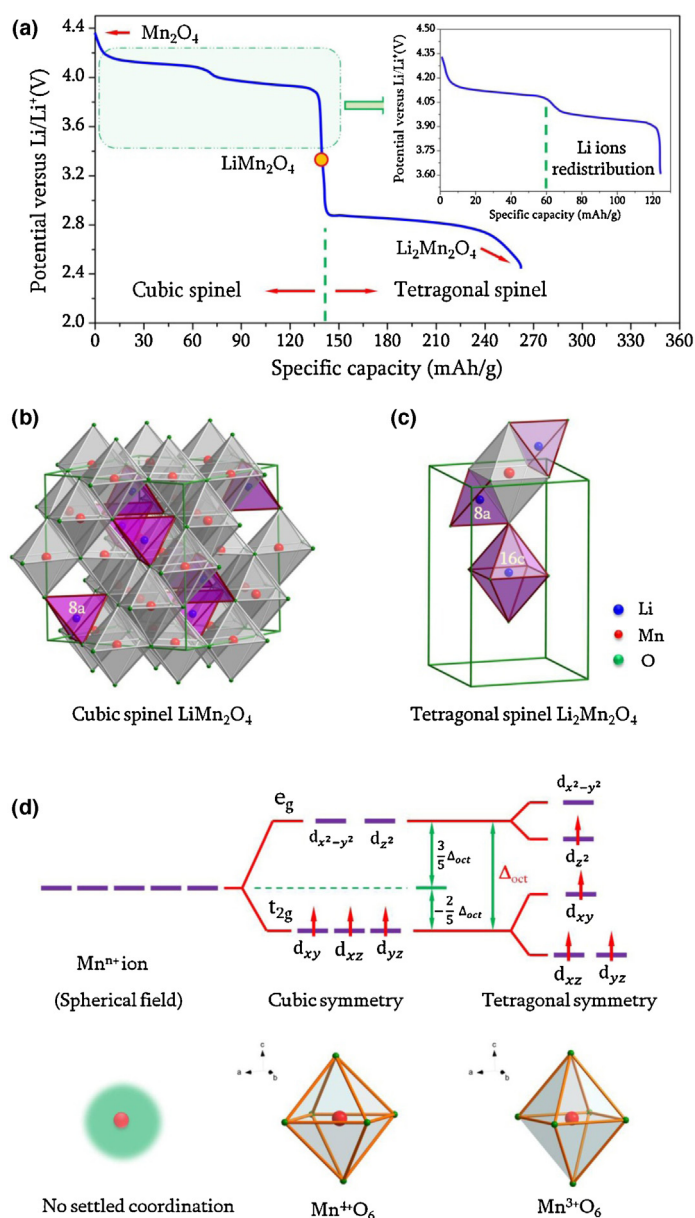


FIGURE 12

(a) Profile of discharge curve in spinel lithium manganate [31]. The potential plateaus are closely correlated with the crystal sites of the Li ions stored. The small potential step near 4 V is associated with the Li-ion redistribution in the cubic structure when the number of Li ions exceeds 0.5. An abrupt potential drop appears when the number of inserted ions exceeds 1 per formula unit. Meanwhile, the crystal structure transforms from cubic to tetragonal. (b) Schematic of cubic spinel and Li ions occupying the spaces of LiO_4 tetrahedrons. (c) Illustration of the connection between polyhedrons in the tetragonal spinel where Li ions start to occupy the 16c octahedrons compared with LiMn_2O_4 . (d) Schematic of splitting of the $3d$ orbitals of Mn ions and the volume change in the MnO_4 octahedrons. The increased energy level reduces the difference in energy of electron transfer, reducing the discharge potential in $\text{Li}_2\text{Mn}_2\text{O}_4$ [72].

face sharing between LiO_4 tetrahedrons and MnO_6 octahedrons [31] (Fig. 12c). This transition from a cubic to a tetragonal crystal structure is accompanied by a 16% increase in the c/a ratio and a 6.5% increase in the unit-cell volume [49,72]. This change in crystal structure is termed as the Jahn–Teller distortion, which arises from the interaction or electrostatic repulsion between the

nonbonding electrons in the p orbitals of the coordinating oxygen anions and the electrons in the d orbitals of the center Mn cation in the oxygen octahedrons. In $\text{Li}_x\text{Mn}_2\text{O}_4$ with $x \leq 1$, Mn ions contain three electrons in the low-energy $3d$ orbitals (the t_{2g} orbitals), one each in d_{xy} , d_{yz} and d_{xz} . The high-energy d_z^2 and $d_x^2 - y^2$ orbitals (the e_g orbitals) do not contain electrons, thus increasing their interacting with p orbitals in oxygen anions. When the number of lithium ions in $\text{Li}_x\text{Mn}_2\text{O}_4$ exceeds 1, the addition of lithium ions will transfer a corresponding electron to the high-energy e_g orbital. This results in a strong electrostatic repulsion between the electrons in the p_z orbitals of the oxygen anion and the electron in the d_z^2 orbital of the Mn cation, which pushes the oxygen anions away from the Mn cations along the z -direction (c -direction in spinel crystal). This repulsive interaction causes the cubic spinel phase to transition to the tetragonal spinel phase. Figure 12d shows the single electron in the e_g orbital of a high-spin Mn^{3+} ($t_{2g}^3 e_g^1$) and the increased c/a ratio in the MnO_6 octahedron [49,75]. In the cubic symmetry, electrons are found in the lower-energy-state t_{2g} orbitals, which requires higher energy to promote or insert one electron than in tetragonal symmetry, wherein the second splitting increases the intrinsic energy of partial electrons. The electron at the highest energy level can participate in the chemical reaction, as it is free to move. Thus, the electron in the d_z^2 orbital is involved in the phase transition, and the reduced difference between the removable electron energy and the Fermi energy of the lithium metal causes the abrupt decline in the potential profile (Fig. 12a). The site energy and electron energy level correspond to the energy difference during the phase transition in the energy storage, which determines the potential that can be achieved.

As mentioned in the section on element selection, Fig. 7a presents an exception. As the atomic numbers of Mn and Fe are 25 and 26, respectively, Fe is more electronegative than Mn. However, olivine LiMnPO_4 displays a higher discharge potential of 4.13 V [127] compared with the 3.43 V of LiFePO_4 [128], as presented in Fig. 13a. Both LiMnPO_4 and LiFePO_4 possess the same crystal structure, with all Li ions occupying the octahedral sites and six coordinating transition metal ions, as shown in the inset of Fig. 13a. As Fe has a larger element number than Mn, Fe attracts electrons in the outer shell more strongly than Mn does, leading to higher energy consumption or release during electron extraction or insertion. However, Fe^{2+} ($3d^6$) requires the electron pairing energy to insert the sixth electron in the t_{2g} orbital, whereas Mn^{2+} ($3d^5$) does not [129]. This difference in energy emerges from the sixth electron present in the higher energy state, as shown in Fig. 13b. As seen from the energy state of Fe and Mn ions, the energy state of the available electrons (denoted by dashed arrows) is lower in Mn^{2+} than in Fe^{2+} . Therefore, as reported, LiMnPO_4 has a higher potential than LiFePO_4 , as more energy could be released or consumed in the discharge or charge process of Mn phosphate [130,131].

Apart from the discharge curves, the profiles of the charge curves are also correlated with the electronic structure of metal ions in the host. During the charge period, Li_2RuO_3 and Li_2MnO_3 show average electrochemical potentials of ~ 3.5 V [136] and ~ 4.8 V [137] vs. Li/Li^+ , respectively. The compound $\text{Li}_2\text{Ru}_{0.5}\text{Mn}_{0.5}\text{O}_3$ appears to be a composite of Li_2RuO_3 and Li_2MnO_3 , displaying two charge plateaus near 3.5 and 4.3 V [138]. The number of reversible Li ions and the average potential increase

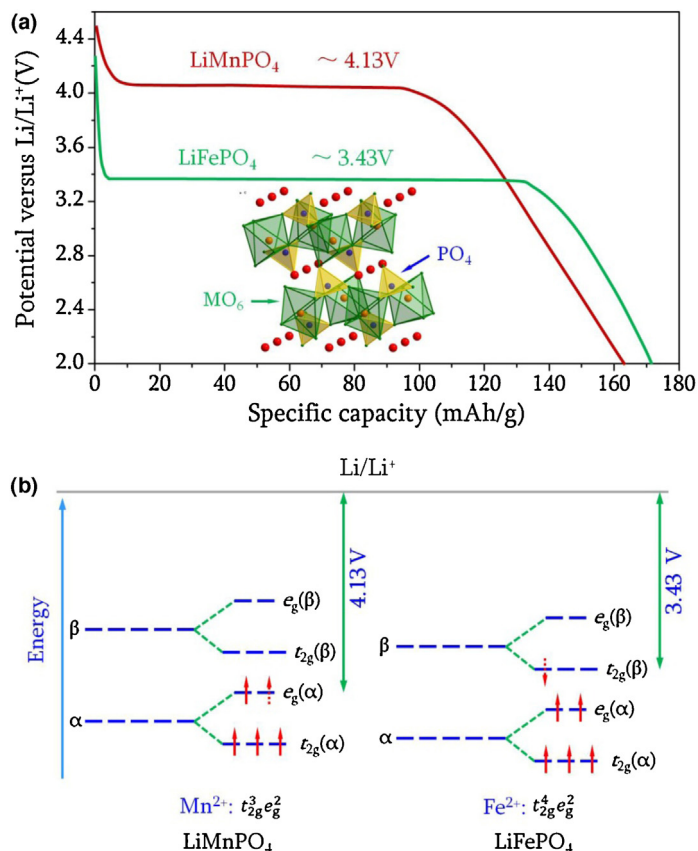


FIGURE 13

(a) Potential profiles of olivine LiFePO_4 and LiMnPO_4 in discharge process, with potential plateaus of 3.43 [132] and 4.13 V [127], respectively. Both materials have the same crystal structures, with MnO_6 octahedrons and PO_4 tetrahedrons [133,134]. (b) Crystal field splitting of the M^{2+} cations in octahedral coordination. The Fe compound delivers a lower voltage vs. Li/Li^+ compared with the Mn compound, because the $\text{Fe}^{2+/3+}$ redox energy shifts due to the pairing energy of the sixth electron in the t_{2g} orbital [129,135].

remarkably in the $\text{Li}_2\text{Ru}_{0.5}\text{Mn}_{0.5}\text{O}_3$ host compared with those of each component. The charge potential is closely related to the energy of the electron's orbital or the band energy. The removable electrons are found in a lower energy state, indicating higher energy consumption when they are promoted. The electron configurations of Mn^{4+} and Ru^{4+} are shown in Fig. 14: four electrons occupy the t_{2g} orbital with a high spin state in Ru^{4+} and three electrons fill the t_{2g} orbital in Mn^{4+} . Li_2RuO_3 exhibits a large $\text{Ru}^{4+}(t_{2g})$ band filled two-thirds, in which the four electrons are fully delocalized over the Ru–Ru and Ru–O bonds. However, Li_2MnO_3 displays a narrower $\text{Mn}^{4+}(t_{2g})$ band with the electrons being localized on the transition metal. This band splits through the coulombic repulsion U_{3d} into one low-lying band filled with three spin-up ($t_{2g\uparrow}$) and one high-lying band of spin-down fully empty ($t_{2g\downarrow}$). Based on the electron configurations of the two compounds, it can be deduced that the Fermi level (E_F) of $\text{Li}_2\text{Ru}_{0.5}\text{Mn}_{0.5}\text{O}_3$ lies within the $\text{Ru}^{4+}(t_{2g})$ band. The Ru^{4+} is then initially oxidized into Ru^{5+} when 0.5 Li are removed from $\text{Li}_2\text{Ru}_{0.5}\text{Mn}_{0.5}\text{O}_3$ with an average potential of approximately 3.5 V. The t_{2g} band of Ru^{5+} then partially overlaps the top of the $\text{O}(2p)$ band, indicating further oxidation of Ru^{5+} in the $\text{Li}_{1.5}\text{Ru}_x\text{Mn}_{1-x}\text{O}_3$ structure to create ' Ru^{6+} ', which can be described as Ru^{5+} with a hole in

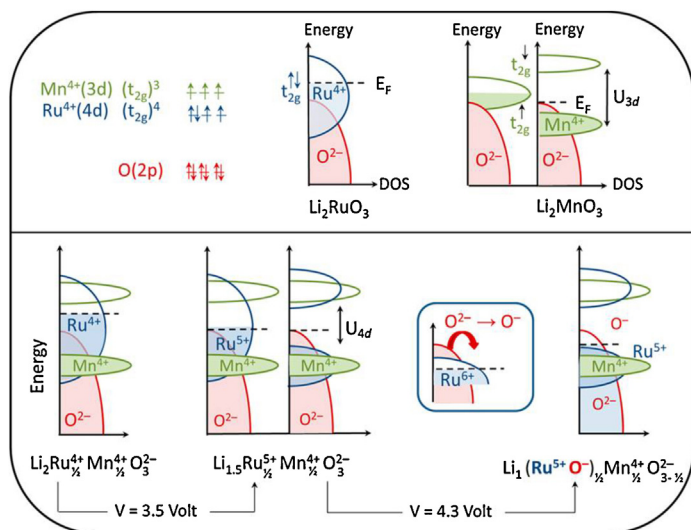


FIGURE 14

Schematic of the density of states (DOS) of Li_2RuO_3 and Li_2MnO_3 (top) and $\text{Li}_{2-x}\text{Ru}_{0.5}\text{Mn}_{0.5}\text{O}_3$ (bottom) in which the Fermi level (E_F) is represented by a horizontal dotted line. $\text{Mn}^{4+}(3d)$, $\text{Ru}^{4+}(4d)$, and $\text{O}^{2-}(2p)$ energy levels indicate the more electronegative character of Ru compared with Mn, and then the stronger Ru(4d)–O(2p) hybridization compared with Mn(3d)–O(2p). The virtual oxidation of Ru^{5+} into Ru^{6+} is shown in the inset [138].

the O^{2-} band. This electron is transferred preferentially when the half-filled t_{2g} band of Ru^{5+} is split by coulombic repulsion U_{4d} . Oxygen vacancies are likely to form with the destabilization of the oxidized O-2p levels. Accounting for some oxygen vacancies, the average potential can reach up to 4.30 V in this process [138]. Therefore, the band structure and the orbital energy influence the energy difference when the electrons are removed, which in turn determines the displayed potential plateaus.

Summary and outlook

As important electrochemical energy storage devices, rechargeable batteries operate via redox reactions in electrode materials. Research into battery technologies has focused on higher energy densities to increase the market demand for electric-powered vehicles with good mileage. The energy density of a device is the product of the specific capacity of the electrode material and the working voltage from the cathode to anode. The specific capacities of certain materials have been exploited to their full extent, but the electrochemical potentials of materials present new research avenues. The voltage of a battery originates from the difference in the electrochemical potentials of the cathode and anode. A higher-potential cathode and a lower-potential anode can be used to assemble a battery with higher voltage. Therefore, the rules and origins of electrochemical potential are essential in the modification or design of a superior electrode. Electronegativity can serve as an initial criterion for selecting suitable elements or polyanions to produce the desired electrochemical potential electrode materials. The site energy of ions and the band energy state of electrons are two main factors that determine the displayed voltage profiles of materials. The crystal field influences the splitting of orbitals, such that the band structure shifts with the change in the local chemical environment. Thus, in a given material, the electrochemical potential can be modified by controlling the matter state, introducing defects, and/or tuning

the microstructures. These rules can aid in the design or modification of cathode or anode materials with the desired electrochemical potential, to assemble high-performance devices with expected voltage and energy density.

Acknowledgements

This work was supported in part by the ‘Thousands Talents’ program for the pioneer researcher and his innovation team, China, and by the National Science Foundation (NSF, CMMI-1030048 and DMR-1505902) and the University of Washington TGIF grant.

References

- [1] J.M. Tarascon, M. Armand, *Nature* 414 (6861) (2001) 359.
- [2] J.B. Goodenough, Y. Kim, *Chem. Mater.* 22 (3) (2010) 587.
- [3] IEA, Transport Energy and CO_2 : Moving toward Sustainability, International Energy Agency (IEA), Paris, France, 2009.
- [4] X. Yin, et al. *Energy Policy* 82 (0) (2015) 233.
- [5] Q.F. Zhang, et al. *Chem. Soc. Rev.* 42 (7) (2013) 3127.
- [6] J.R. Miller, P. Simon, *Science* 321 (5889) (2008) 651.
- [7] K. Kalyanasundaram, M. Gratzel, *J. Mater. Chem.* 22 (46) (2012) 24190.
- [8] G.M. Shafullah, et al. *Renew. Sustain. Energy Rev.* 20 (0) (2013) 306.
- [9] R. Singh, A.D. Setiawan, *Renew. Sustain. Energy Rev.* 22 (0) (2013) 332.
- [10] P. Würfel, *Physics of Solar Cells: From Basic Principles to Advanced Concepts*, Wiley-VCH, 2009.
- [11] P. Simon, et al. *Science* 343 (6176) (2014) 1210.
- [12] P. Simon, Y. Gogotsi, *Nat. Mater.* 7 (11) (2008) 845.
- [13] M. Winter, R.J. Brodd, *Chem. Rev.* 104 (10) (2004) 4245.
- [14] M. Armand, J.M. Tarascon, *Nature* 451 (7179) (2008) 652.
- [15] Z. Yang, et al. *Chem. Rev.* 111 (5) (2011) 3577.
- [16] P. Ruetschi, *J. Power Sources* 2 (1) (1977) 3.
- [17] D. Larcher, J.M. Tarascon, *Nat. Chem.* 7 (1) (2015) 19.
- [18] D. Aurbach, et al. *Adv. Mater.* 19 (23) (2007) 4260.
- [19] G.L. Soloveichik, *Annu. Rev. Chem. Biomol.* 2 (1) (2011) 503.
- [20] J.R. Owen, *Chem. Soc. Rev.* 26 (4) (1997) 259.
- [21] N. Nitta, et al. *Mater. Today* 18 (5) (2015) 252.
- [22] J.B. Goodenough, *Acc. Chem. Res.* 46 (5) (2012) 1053.
- [23] N. Yabuuchi, et al. *Chem. Rev.* 114 (23) (2014) 11636.
- [24] M.H. Han, et al. *Energy Environ. Sci.* 8 (1) (2015) 81.
- [25] M.D. Slater, et al. *Adv. Funct. Mater.* 23 (8) (2013) 947.
- [26] P. Saha, et al. *Prog. Mater. Sci.* 66 (0) (2014) 1.
- [27] M.M. Huie, et al. *Coord. Chem. Rev.* 287 (0) (2015) 15.
- [28] Q. Li, N.J. Bjerrum, *J. Power Sources* 110 (1) (2002) 1.
- [29] M.-C. Lin, et al. *Nature* 520 (7547) (2015) 324.
- [30] M.S. Whittingham, *Chem. Rev.* 104 (10) (2004) 4271.
- [31] J.B. Goodenough, K.-S. Park, *J. Am. Chem. Soc.* 135 (4) (2013) 1167.
- [32] R. Massé, et al. *Sci. China Mater* 58 (9) (2015) 715.
- [33] H.D. Yoo, et al. *Mater. Today* 17 (3) (2014) 110.
- [34] A. Yoshino, *Angew. Chem. Int. Ed.* 51 (24) (2012) 5798.
- [35] S.R. Bottone, *Galvanic Batteries, Their Theory, Construction and Use, Comprising Primary, Single and Double Fluid Cells. Secondary and Gas Batteries*, Nabu Press, 2010.
- [36] H. Wu, Y. Cui, *Nano Today* 7 (5) (2012) 414.
- [37] M.N. Obrovac, V.L. Chevrier, *Chem. Rev.* 114 (23) (2014) 11444.
- [38] M. Zhang, et al. *Int. Mater. Rev.* 60 (6) (2015) 330.
- [39] S. Goriparti, et al. *J. Power Sources* 257 (0) (2014) 421.
- [40] Y. Wang, G. Cao, *Chem. Mater.* 18 (12) (2006) 2787.
- [41] M. Winter, et al. *Adv. Mater.* 10 (10) (1998) 725.
- [42] A.S. Arico, et al. *Nat. Mater.* 4 (5) (2005) 366.
- [43] M. Noel, V. Suryanarayanan, *J. Power Sources* 111 (2) (2002) 193.
- [44] A.D. Roberts, et al. *Chem. Soc. Rev.* 43 (13) (2014) 4341.
- [45] E. Antolini, *Solid State Ionics* 170 (3–4) (2004) 159.
- [46] J. Wang, X. Sun, *Energy Environ. Sci.* 8 (4) (2015) 1110.
- [47] L.-X. Yuan, et al. *Energy Environ. Sci.* 4 (2) (2011) 269.
- [48] R. Koksang, et al. *Solid State Ionics* 84 (1–2) (1996) 1.
- [49] J.-K. Park, *Principles and Applications of Lithium Secondary Batteries*, Wiley-VCH Germany, 2012.
- [50] M.S. Islam, C.A. Fisher, *J. Chem. Soc. Rev.* 43 (1) (2014) 185.
- [51] D.P. Dubal, et al. *Chem. Soc. Rev.* 44 (1) (2015) 1777.
- [52] H.D. Abruna, Y. Kiya, I.C. Henderson, *Phys. Today* 61 (12) (2008) 43.

- [53] R. Mukherjee, et al. *Nano Energy* 1 (4) (2012) 518.
- [54] P. Roy, S.K. Srivastava, *J. Mater. Chem. A* 3 (6) (2015) 2454.
- [55] W. Shi, et al. *J. Phys. Chem. C* 116 (51) (2012) 26685.
- [56] J. Wang, X. Sun, *Energy Environ. Sci.* 5 (1) (2012) 5163.
- [57] L. Su, et al. *Nanoscale* 3 (10) (2011) 3967.
- [58] I. Lahiri, W. Choi, *Crit. Rev. Solid State* 38 (2) (2013) 128.
- [59] A.L.M. Reddy, et al. *Adv. Mater.* 24 (37) (2012) 5045.
- [60] N. Brun, et al. *J. Phys. Chem. C* 116 (1) (2012) 1408.
- [61] M. Srivastava, et al. *Nanoscale* 7 (11) (2015) 4820.
- [62] V. Augustyn, et al. *Energy Environ. Sci.* 7 (5) (2014) 1597.
- [63] D. Li, H. Zhou, *Mater. Today* 17 (9) (2014) 451.
- [64] A. Van der Ven, et al. *Acc. Chem. Res.* 46 (5) (2013) 1216.
- [65] F. Bonaccorso, et al. *Science* 347 (2015) 6217.
- [66] M.S. Whittingham, *Chem. Rev.* 114 (23) (2014) 11414.
- [67] E. Uchaker, G. Cao, *Nano Today* 9 (4) (2014) 499.
- [68] L. Mai, et al. *Chem. Rev.* 114 (23) (2014) 11828.
- [69] N. Liu, et al. *Front. Phys.* 9 (3) (2014) 323.
- [70] D. Aurbach, et al. *Nature* 407 (6805) (2000) 724.
- [71] D. Kundu, et al. *Angew. Chem. Int. Ed.* 54 (11) (2015) 3431.
- [72] G.P. Gholam Abbas Nazri, *Lithium Batteries: Science and Technology*, Kluwer Academic Publishers, 2003.
- [73] V.A. Agubra, J.W. Fergus, *J. Power Sources* 268 (0) (2014) 153.
- [74] J.B. Goodenough, *Energy Environ. Sci.* 7 (1) (2014) 14.
- [75] H. Berg, et al. *J. Mater. Chem.* 9 (11) (1999) 2813.
- [76] Atkins, *Physical Chemistry*, 7th ed., W. H. Freeman, 2001.
- [77] M. Tang, et al. *Annu. Rev. Mater. Res.* 40 (1) (2010) 501.
- [78] B.C. Melot, J.M. Tarascon, *Acc. Chem. Res.* 46 (5) (2013) 1226.
- [79] M. Zhi, et al. *Nanoscale* 5 (1) (2013) 72.
- [80] B. Liang, et al. *J. Power Sources* 267 (2014) 469.
- [81] C. Delmas, et al. *Solid State Ionics* 69 (3–4) (1994) 257.
- [82] S. Luo, et al. *Adv. Mater.* 24 (17) (2012) 2294.
- [83] V. Augustyn, et al. *Nat. Mater.* 12 (6) (2013) 518.
- [84] B. Wang, et al. *Mater. Today* 15 (12) (2012) 544.
- [85] C. Masquelier, L. Croguennec, *Chem. Rev.* 113 (8) (2013) 6552.
- [86] G. Hautier, et al. *Chem. Mater.* 23 (15) (2011) 3495.
- [87] A. Jain, et al. *Phys. Chem. Chem. Phys.* 17 (8) (2015) 5942.
- [88] A. Manthiram, J.B. Goodenough, *J. Power Sources* 26 (3–4) (1989) 403.
- [89] G.G. Amatucci, N. Pereira, *J. Fluorine Chem.* 128 (4) (2007) 243.
- [90] T. Nakajima, *J. Fluorine Chem.* 149 (0) (2013) 104.
- [91] P. Barpanda, et al. *Nat. Commun.* 5 (2014) 1.
- [92] L. Zhang, et al. *Nano Lett.* 15 (1) (2015) 656.
- [93] Y.-Z. Zheng, et al. *J. Mater. Chem. A* 3 (5) (2015) 1979.
- [94] P.G. Bruce, et al. *Angew. Chem. Int. Ed.* 47 (16) (2008) 2930.
- [95] F. Jiao, P.G. Bruce, *Adv. Mater.* 19 (5) (2007) 657.
- [96] M. Okubo, et al. *J. Am. Chem. Soc.* 129 (23) (2007) 7444.
- [97] Y.-G. Guo, et al. *Adv. Mater.* 20 (15) (2008) 2878.
- [98] Y.-M. Chiang, et al., *Physical Ceramics: Principles for Ceramic Science and Engineering*, Wiley, 1996.
- [99] R. Yazami, *Nanomaterials for Lithium-Ion Batteries: Fundamentals and Applications*, CRC Press, Taylor & Francis Group, 2013.
- [100] A. Manthiram, et al. *Energy Environ. Sci.* 7 (4) (2014) 1339.
- [101] S.P. Ong, et al. *Energy Environ. Sci.* 4 (9) (2011) 3680.
- [102] P. He, et al. *J. Mater. Chem.* 22 (9) (2012) 3680.
- [103] S.-J. Hwang, et al. *Chem. Mater.* 12 (7) (2000) 1818.
- [104] H. Ji, et al. *ACS Sustain. Chem. Eng.* 2 (3) (2014) 359.
- [105] A.R. Armstrong, P.G. Bruce, *Nature* 381 (6582) (1996) 499.
- [106] A.S. Andersson, J.O. Thomas, *J. Power Sources* 97–98 (0) (2001) 498.
- [107] T. Ohzuku, A. Ueda, *J. Electrochem. Soc.* 141 (11) (1994) 2972.
- [108] T.-F. Yi, et al. *J. Mater. Chem. A* 3 (11) (2015) 5750.
- [109] J. Lee, et al. *Science* 343 (6170) (2014) 519.
- [110] R. Chen, et al. *Adv. Energy Mater.* 5 (9) (2015) 1401814.
- [111] P. Saha, et al. *J. Electrochem. Soc.* 161 (4) (2014) A593.
- [112] K.R. Kganyago, et al. *Phys. Rev. B* 67 (10) (2003) 104103.
- [113] E. Levi, et al. *J. Electroceram.* 22 (1–3) (2007) 13.
- [114] D. Liu, et al. *J. Phys. Chem. C* 115 (11) (2011) 4959.
- [115] D. Liu, et al. *J. Mater. Chem.* 19 (46) (2009) 8789.
- [116] C. Zhang, et al. *Adv. Funct. Mater.* 25 (23) (2015) 3497.
- [117] E. Uchaker, et al. *J. Mater. Chem. A* 2 (43) (2014) 18208.
- [118] B.P. Hahn, et al. *Acc. Chem. Res.* 46 (5) (2013) 1181.
- [119] Y. Yin, et al. *Chem. Commun.* 48 (15) (2012) 2137.
- [120] O.B. Chae, et al. *Chem. Mater.* 26 (20) (2014) 5874.
- [121] Y. Liu, et al. *Nano Lett.* 12 (11) (2012) 5664.
- [122] Y. Fang, et al. *Nano Lett.* 14 (6) (2014) 3539.
- [123] C. Zhu, et al. *Nano Lett.* 14 (9) (2014) 5342.
- [124] J.R. Dahn, et al. *Science* 270 (5236) (1995) 590.
- [125] Y. Idota, et al. *Science* 276 (5317) (1997) 1395.
- [126] http://en.wikipedia.org/wiki/Crystal_field_theory.
- [127] D. Choi, et al. *Nano Lett.* 10 (8) (2010) 2799.
- [128] Z. Lu, et al. *Chem. Mater.* 23 (11) (2011) 2848.
- [129] A. Gutierrez, et al. *Chem. Mater.* 25 (20) (2013) 4010.
- [130] V. Aravindan, et al. *J. Mater. Chem. A* 1 (11) (2013) 3518.
- [131] D. Jugovic, D. Uskokovic, *J. Power Sources* 190 (2) (2009) 538.
- [132] Y. Wang, et al. *Energy Environ. Sci.* 4 (3) (2011) 805.
- [133] S. Geller, J.L. Durand, *Acta Crystallogr.* 13 (4) (1960) 325.
- [134] M.A.E. Sanchez, et al. *Solid State Ionics* 177 (5–6) (2006) 497.
- [135] T. Muraliganth, A. Manthiram, *J. Phys. Chem. C* 114 (36) (2010) 15530.
- [136] A.C.W.P. James, J.B. Goodenough, *J. Solid State Chem.* 74 (2) (1988) 287.
- [137] J.R. Croy, et al. *Chem. Mater.* 26 (24) (2014) 7091.
- [138] M. Sathiyaraj, et al. *Chem. Mater.* 25 (7) (2013) 1121.